Energy & Environmental Science

ROYAL SOCIETY OF CHEMISTRY

PAPER

View Article Online
View Journal

Cite this: DOI: 10.1039/d6ee01132b

Efficient and stable electrochemical carbon capture *via* integrated CO_2 absorption and regeneration

Zhiwei Fang, *[a] Junwei Zhang,[a] Peng Zhu,[a] Zhou Yu,[a] Ahmad Elgazzar,[a] Juan Wang,[a] Wei Ping Lam[a] and Haotian Wang *[abcde]

Received 18th February 2026,
Accepted 13th May 2026

DOI: 10.1039/d6ee01132b

rsc.li/ees

Carbon capture in electrochemical cells generally relies on the local pH difference at the two electrodes, which results in high pH overpotentials and high energy consumption. Here, we integrate CO_2 absorption and *in situ* CO_2/sorbent regeneration steps in a single electrochemical reactor for reduced energy consumption, a simplified process design, and improved reactor stability. By directly feeding the carbon source into the cathode chamber while performing the CO_2 and sorbent regeneration electrolysis from (bi)carbonate solutions, we successfully demonstrate in-cell carbon capture and the mitigation of local pH elevation, which effectively reduces the pH overpotentials and enhances the electron efficiency. Our system enables predominant bicarbonate-based CO_2 capture under point-source conditions, requiring only ~48 kJ mol^{-1} CO_2 for onset capture and ~180 kJ mol^{-1} CO_2 at 100 mA cm^{-2}. This strategy achieves high sorbent utilization efficiency, improved electron utilization, and reduced energy consumption, enabling stable carbon capture operation (3.5% CO_2 concentration input) at 50 mA cm^{-2} for over 1000 hours, with the cation transport efficiency maintained above 80%.

Broader context

Decarbonizing energy and industrial systems require carbon capture technologies that combine low energy consumption, operational durability, and scalable process integration. Electrochemical carbon capture has emerged as a promising alternative to thermally driven regeneration because it can directly couple electricity with sorbent regeneration under mild conditions. However, many existing systems rely on large pH gradients between electrodes to release CO_2, which inherently generates significant pH overpotentials, reduces electron efficiency, and increases the overall energy demand. Consequently, reactor architecture and interfacial transport management have become critical challenges for the practical deployment of electrochemical carbon capture. Here, we address this challenge through an integrated reactor design that couples CO_2 absorption with *in situ* electrochemical CO_2/sorbent regeneration while promoting bicarbonate-mediated capture pathways. This configuration moderates local pH accumulation and maintains effective ionic transport, thereby reducing pH-related energy losses and improving sorbent utilization and electron efficiency during continuous operation. Stable performance at low CO_2 concentrations further supports applicability to flue gas and dilute carbon streams. More broadly, this work demonstrates how reactor-level integration and microenvironment engineering can advance electrically driven carbon capture toward scalable and energy-efficient carbon management technologies.

Introduction

As fossil fuels remain a significant part of the global energy production and industrial processes, the effective mitigation of continuous carbon pollution from different point sources into the atmosphere has become more urgent than ever. Captured CO_2 can be converted into value-added chemicals, such as carbonates or fuels, or transported to suitable storage sites, where it is securely stored to prevent it from re-entering the atmosphere.[1–3] In recent years, beyond point source capture, direct air capture has started playing an important role in capturing CO_2 directly from the atmosphere, offering the flexibility to install facilities near renewable energy sources and geological storage sites and improving the reliability of carbon feedstock supply chains for certain chemical manufacturing processes.[4–7]

Recent advancements in carbon capture, utilization, and storage (CCUS) technologies have led to significant developments

[a] Department of Chemical and Biomolecular Engineering, Rice University, Houston, TX, 77005, USA. E-mail: zf20@rice.edu, htwang@rice.edu
[b] Department of Chemistry, Rice University, Houston, TX, 77005, USA
[c] Department of Materials Science and NanoEngineering, Rice University, Houston, TX, 77005, USA
[d] Rice Advanced Materials Institute, Rice University, Houston, Texas, 77005, USA
[e] Rice WaTER Institute, Rice University, Houston, Texas, 77005, USA

in new capture materials and processes, but scaling them up for industrial applications remains challenging.[7–9] The widely used chemical absorption method, based on organic amines, is effective but suffers from several major limitations, including solvent degradation and equipment corrosion, highlighting the urgent need for more efficient and stable alternatives. In addition, conventional amine-based CCS systems still require substantial energy input, with parasitic electrical demands of ~30–50 kJ mol^{-1} CO_2 and thermal regeneration energies reaching ~2–4 GJ per ton CO_2 (88–176 kJ mol^{-1} CO_2).[9–12] Inorganic alkaline solutions, particularly hydroxide-based systems, present a promising solution for carbon capture owing to their high capture efficiency, low material costs due to the abundance of alkali metals, high chemical stability, and good scalability for industrial use.[13] However, due to the high chemical stability of the alkali metal carbonates formed when CO_2 reacts with hydroxides (such as Na_2CO_3 or K_2CO_3), cation exchange with Ca^{2+} is often required to produce $CaCO_3$, which is then subjected to high-temperature (~900 °C) calcination for CO_2 release and sorbent regeneration. While this calcination step is a well-established and widely scaled industrial process, particularly in cement production, its high energy demand and reliance on natural gas as a thermal energy source present significant barriers to large-scale deployment (Fig. 1a).[3]

Emerging electrochemical methods present a potential breakthrough for addressing the above-mentioned challenges in current carbon capture technologies.[14–19] Instead of relying on high-temperature calcination processes to split metal ions from carbonates for alkaline and CO_2 regeneration, novel electrochemical processes have been demonstrated to effectively split carbonate salts into alkaline sorbents and high-purity CO_2 during room-temperature and ambient-pressure operations (Fig. 1b).[15,20] Compared with other electrochemical carbon capture technologies using redox-active organic molecules,[9–11] the electrochemical splitting of alkali metal (bi)carbonates ($NaHCO_3$ or $KHCO_3$) avoids the use of hazardous, air-sensitive, or poor-cycling-stability materials. Our recent work on a three-chamber cation exchange membrane (CEM)-based porous solid electrolyte (PSE) reactor demonstrated that electrochemical regeneration can efficiently produce hydroxide and recover CO_2 from absorbents, showing significant advantages compared to conventional thermal regeneration processes.[21–23] By flowing (bi)carbonate solutions through the middle PSE layer while carrying out redox reactions at the cathode and anode, the reactor continuously acidifies the carbonate solution, regenerating high-purity CO_2 from the PSE layer while simultaneously basifying the cathode chamber as cations are drawn into it.[24,25] However, there are still challenges for this approach to be practically implemented.[19,26] For instance, in air contactors, the carbon capture process typically halts at the carbonate phase due to the slow reaction kinetics of bicarbonate formation. Regenerating CO_2 from carbonates requires

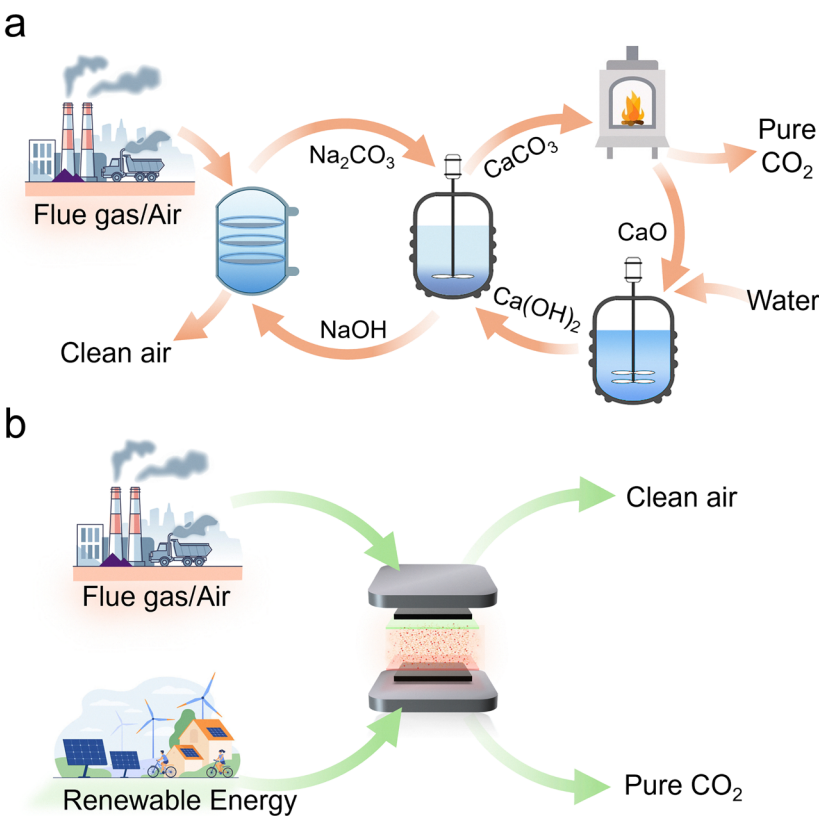

Fig. 1 Comparison between calcium looping and electrochemical CO_2 capture. (a) Schematic of the pilot-scale CO_2 capture process *via* calcium carbonate looping. (b) Schematic of the electrochemical CO_2 capture from flue gas or air using our solid electrolyte reactor for complete carbon capture.

twice the number of electrons compared to bicarbonates, as each carbonate involves the transfer of two protons (H^+).[23,27] This reduces electron efficiency and increases energy consumption.[23,27,28] Another challenge is that although a sharp pH gradient between the cathode and anode is needed to generate a chemical potential difference that can be used for CO_2 and sorbent regeneration, this pH difference also contributes to large pH overpotentials, which dramatically increase the energy consumption.[23] Therefore, addressing these drawbacks is crucial to further improve the feasibility and energy efficiency of this electrochemical carbon capture method.

In this work, we demonstrate an integrated carbon absorption and regeneration process in a single PSE reactor unit for significantly reduced energy consumption and improved operational stability. By directly feeding the CO_2 source gas, typically containing O_2, into the cathode chamber while performing an oxygen reduction reaction (ORR), we leverage the locally high-concentration hydroxides at the cathode/CEM interface for efficient CO_2 absorption and hydroxide utilization. Compared with in-cell alkaline generation, followed by out-of-cell carbon absorption, this in-cell CO_2 capture design not only simplifies the overall carbon capture process design by eliminating the CO_2 absorption unit, but also, more importantly, effectively neutralizes the interfacial pH for significantly lowered pH overpotentials and improved Na^+ transport efficiency (t_{Na+}). Specifically, at an operating current density of 50 mA cm^{-2} and a 10% CO_2 concentration for carbon capture, the cell voltage decreases from 1.70 to 1.51 V, while t_{Na+} increases from 92.6% to 96.0%, representing a 15% improvement in energy consumption. By carefully matching the operating current density with the input CO_2 concentration, we capture carbon from point-source streams (1% to 20%), predominantly in the form of bicarbonate, which delivers ~48 kJ $mol_{CO_2}^{-1}$ for onset capture and ~180 kJ $mol_{CO_2}^{-1}$ at 100 mA cm^{-2} (under a 10% CO_2 feed). While performing the same ORR/OER redox electrolysis, this new design requires a ~53% lower energy input compared to the previously reported anion exchange membrane-proton exchange membrane (AEM-PEM) PSE reactor system,[26] which predominantly captures CO_2 *via* the formation of carbonates, due to significantly enhanced electron efficiency. More importantly, due to the robust chemical stability of CEMs, our CEM-based PSE carbon capture reactor shows excellent long-term reliability, delivering an ultra-stable carbon capture operation at 50 mA cm^{-2} for over 1000 hours while maintaining a transport efficiency of >85% and an electron efficiency of >65%. Notably, our approach is also effective for direct air capture, with an onset energy consumption of ~52 kJ $mol_{CO_2}^{-1}$ and 203 kJ $mol_{CO_2}^{-1}$ at 5 mA cm^{-2}, as well as an electron efficiency of over 70%. The operational flexibility of the integrated system enables carbon capture to be performed near renewable energy sources, providing a pathway to improving the overall energy efficiency in CCUS applications.

Results and discussion

Integrated electrochemical CO_2 absorption and regeneration design

Our system can be implemented for different CO_2 sources, ranging from flue gas capture to DAC. The overall process of the electrochemical CO_2 absorption and regeneration loop is illustrated in Fig. 2a. The loop begins with the reduction of oxygen to generate hydroxide ions (OH^-) at the cathode, which react with CO_2 from the gas feed to form (bi)carbonates. These captured carbon species then flow to a buffer chamber, where they react with protons generated at the anode to release high-purity CO_2 gas. Meanwhile, oxygen is regenerated at the anode and recirculated to the cathode to complete the cycle. Through this loop, CO_2 from flue gas or air is continuously separated

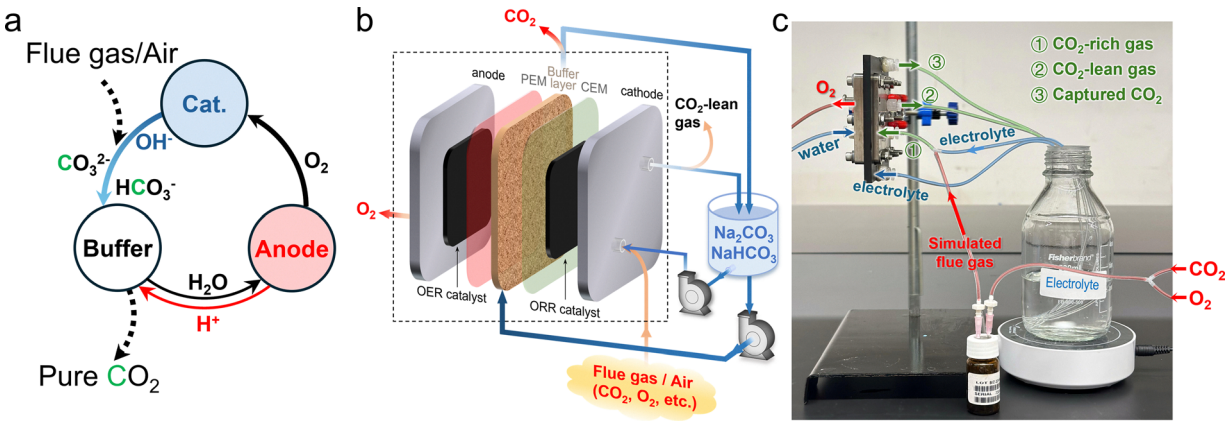

Fig. 2 Schematic and demonstration of electrochemical CO_2 capture in a solid electrolyte reactor. (a) Process of the electrochemical CO_2 absorption and regeneration loop from flue gas or air in our solid electrolyte reactor. (b) Schematic of the electrochemical carbon capture and CO_2 regeneration process. The terms PEM and CEM are used in this work to distinguish their functional roles: PEM is applied when H^+ transport is desired, while CEM is used when Na^+ is the target cation. (c) Lab-scale set-up for electrochemical carbon capture and pure CO_2 regeneration (pump and air flow meters ignored for simplicity). Green line 1: pure CO_2 gas/liquid mixture (pH: near-neutral or acidic); green line 2: CO_2-lean gas/absorbent mixture (pH: near-neutral or basic); green line 3: CO_2-rich gas/liquid mixture (pH: near-neutral or acidic); blue line: liquid (required by the pump to control the liquid flow rate); and red line: gas (required by the airflow meter to control the gas flow rate).

into pure CO_2 without any consumption or generation of other chemicals.

The process is facilitated by a three-chamber electrolyzer architecture consisting of a cathode, a PEM-separated buffer chamber packed with a porous solid electrolyte (PSE) layer, and an anode (Fig. 2b). At the anode, the oxygen evolution reaction (OER, $H_2O - 2e^- \rightarrow 2H^+ + \frac{1}{2}O_2$) supplies both protons and oxygen, catalyzed by an OER catalyst. The oxygen produced is recirculated to the cathode, where the oxygen reduction reaction (ORR) occurs on catalysts such as Pt/C or Co single-atom catalysts.[29] The ORR generates OH^-, which reacts with CO_2 to form bicarbonate ($CO_2 + \frac{1}{4}O_2 + \frac{1}{2}H_2O + e^- \rightarrow HCO_3^-$) or carbonate ($CO_2 + \frac{1}{2}O_2 + e^- \rightarrow CO_3^{2-}$), depending on the capture conditions. The protons produced at the anode transport across the PEM into the middle buffer chamber, where (bi)carbonate species react with H^+ to regenerate CO_2 and water ($CO_3^{2-} + H^+ \rightarrow HCO_3^-$, $HCO_3^- + H^+ \rightarrow CO_2 + H_2O$). Cations migrate from the buffer chamber to the cathode across the CEM to balance the charge. Overall, the electrolyzer converts CO_2 from flue gas or air into high-purity CO_2 (net reaction: CO_2 (flue gas or air) $\rightarrow$ CO_2 (pure)) without net consumption of chemical sorbents, enabled by coordinated flow, ion transport, and chemical transformations within the cell. The photograph of the electrochemical cell design is provided in Fig. 2c.

For a typical CO_2 regeneration from (bi)carbonates, we compared three different operation cases with different pH overpotentials, as shown in Fig. 3. In all three cases, the CEM is required to separate the middle chamber and cathode compartment for selective Na^+ transport (Fig. S4). The CEM is essential to suppress uncontrolled ion crossover, which would otherwise eliminate the pH gradient and disrupt the decoupled capture–regeneration mechanism, resulting in significant performance degradation. In the first scenario, we consider independent CO_2 absorption and regeneration steps. In this case, we do not flow CO_2-containing gas into the cathode chamber, resulting in the generation of alkaline sorbents, while a high-purity CO_2 gas stream is regenerated inside the PSE layer from (bi)carbonates. The regenerated alkaline sorbent then flows to the downstream air contactors for the carbon capture process. In this case, we create a sharp pH difference between the anode and cathode interface, and we will have the largest pH overpotential during electrolysis operation. In the second case, we include CO_2 in the cathode inlet gas composition (containing both O_2 and CO_2), which reacts with the in situ-generated hydroxide ions right at the cathode/membrane interface to form (bi)carbonates, effectively decreasing the cathode interfacial pH. These carbon-containing ions flow to the middle chamber and react with protons from the anode to release pure CO_2. In this case, the carbon absorption and carbon regeneration steps are integrated and happen simultaneously, and the pH difference

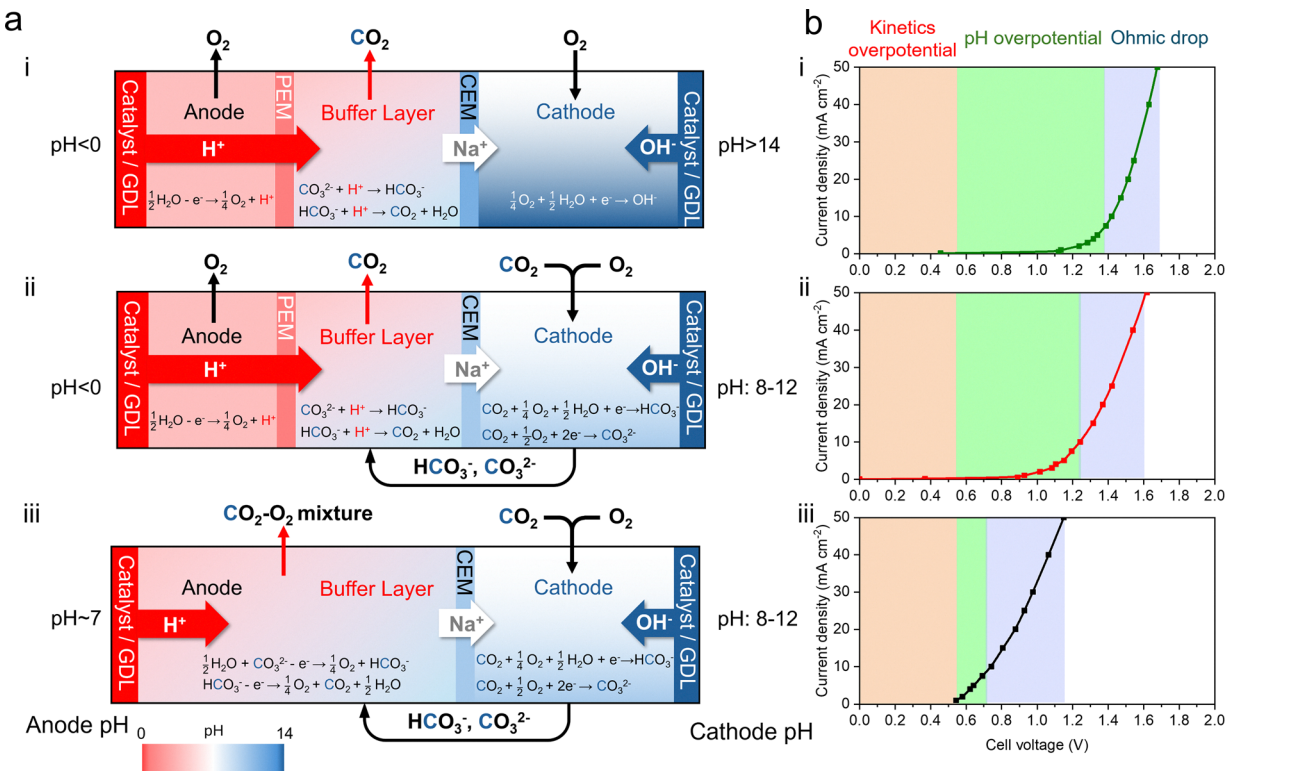

Fig. 3 Electrolyzer configuration optimization. (a) Schematic illustration of ion transport in three electrolyzer configurations for the integrated electrochemical carbon absorption and regeneration process: (i) 3-chamber PSE electrolyzer with a pure O_2 feed; (ii) 3-chamber PSE electrolyzer with a CO_2–O_2 mixed feed; and (iii) 2-chamber PSE electrolyzer with a CO_2–O_2 mixed feed. (b) Corresponding cell voltage breakdowns for configurations (i)–(iii).

between the cathode and anode is reduced due to CO_2-(bi)carbonate buffering effects. In the third scenario, because the cathode side interfacial pH now has limited room to be further lowered, we could consider adjusting the anode pH by removing the PEM and forming a two-chamber reactor system. When the PEM in the anode is removed, OER-derived protons are effectively buffered by (bi)carbonates in the PSE layer to form carbonic acid and release CO_2. This will result in an elevated pH at the anode interface, further lowering the pH overpotential of the cell. However, the penalty here is the mixture of the regenerated CO_2 stream with the O_2 stream from the OER, which necessitates additional separation processes to isolate pure CO_2 and O_2 for subsequent use or storage. While the CO_2 concentration (80% when considering regenerating bicarbonate, $HCO_3^- + \frac{1}{2}H_2O - e^- \rightarrow CO_2 + H_2O + \frac{1}{2}O_2$) is significantly improved compared to the cathode feed, this operational mode may find limited application scenarios.

The practical cell voltage ($V_{cell,practical}$) can be expressed using the following equation:

$$V_{cell,practical} = \frac{2.303 \times RT}{F}(pH_{basified} - pH_{acidified}) + V_{rxn,overpotential} + iR, \quad (1)$$

where R is the universal gas constant (8.3144 J K^{-1} mol^{-1}), T is the temperature, and F is the Faraday constant (9.6485 × 10^4 C mol^{-1}). This equation, derived from the Nernst equation, accounts for the pH gradient across the cell. $pH_{basified}$ refers to the pH at the cathode interface in the basified compartment, while $pH_{acidified}$ represents the pH at the anode interface in the acidified compartment.

This equation incorporates three main contributing factors: (1) pH overpotential, (2) catalyst overpotentials for the anodic and cathodic half-reactions (activation energy barriers), and (3) the internal resistance (ohmic drop) of the cell. In this study, $V_{rxn,overpotential}$ refers to the overpotentials of anodic OER and cathodic ORR catalysts, while the cell resistance (iR) includes PSE resistance, membrane resistance, and electrode resistance.

For pure CO_2 and sorbent regeneration (case (i)), the PEM and CEM are both utilized, with a pure O_2 feed at the cathode, resulting in a highly acidic interface at the anode and a strongly basic flow at the cathode. In case (ii), following the integration of CO_2 absorption into the system, the pH of the cathode flow can decrease due to the direct reaction between the generated OH^- and CO_2. The pH can be reduced to 8–10 if the captured product is bicarbonate or to 11–13 if the product is carbonate. In case (iii), the anode pH can significantly increase after removing the PEM at the anode side. Without the PEM acting as a proton channel, the proton concentration at the anode gradually decreases as protons react with (bi)carbonate ions.

Effects of In-Cell CO_2 absorption on PSE electrolyzer performance

To validate the hypothesis from Fig. 3 and investigate how the CO_2 concentration and current density affect the performance of the PSE electrolyzer, we varied these parameters and evaluated their impact on key metrics such as cell voltage, ion transport efficiency, and pH changes. Fig. 4a illustrates the current–voltage (*IV*) curve and sodium transport efficiency of a three-chamber PSE reactor supplied with a 10% CO_2 feed at the cathode (case (ii)). At a current density of 50 mA cm^{-2}, the cell voltage is approximately 1.51 V, while at 100 mA cm^{-2}, the cell voltage increases to 1.75 V. Compared with systems where carbon capture takes place outside the electrolyzer (pure O_2 feed), the cell voltage is higher than that of the integrated system. This increase can be attributed to the increased cathodic pH, as shown in eqn (1), resulting from the existence of hydroxides instead of (bi)carbonates. Additionally, the separated system shows a slightly lower cation transport efficiency (Fig. S6 and S7), which can be attributed to the higher proton crossover from the middle chamber competing with Na^+ (or K^+) transport at high pH in the absence of CO_2. The energy consumption for carbon capture is displayed in Fig. 4b, demonstrating that the presence of CO_2 at the cathode lowers the energy inputs due to the synergistic effect of the lowered cell voltage and improved Na^+ transport efficiency. The onset energy consumption of 10% CO_2 capture is approximately 50 kJ $mol_{CO_2}^{-1}$, with the average consumption ranging from 140 to 190 kJ $mol_{CO_2}^{-1}$ at 50 mA cm^{-2}.

According to eqn (2), only the cathodic pH ($pH_{cat.}$) is relevant to the CO_2 concentration. Therefore, the relationship between the cell voltage and $pH_{cat.}$ was further investigated. Based on the Nernst equation, the cell voltage difference (ΔV) between CO_2-free (case (i) in Fig. 3a) and CO_2-fed (case (ii) in Fig. 3a) cathodic conditions is given by the following equation:

$$\Delta V = \frac{2.303 \times RT}{F}(pH_{cat,i} - pH_{cat,ii}). \quad (2)$$

Therefore, the cathodic pH difference ($\Delta pH_{cathode} = pH_{cat,i} - pH_{cat,ii}$) between the two conditions can be calculated using the equation $\Delta pH_{cat.} = \frac{\Delta V}{0.0591}$. As shown in Fig. 4c and Fig. S8, the pH under 10%-CO_2-fed conditions decreases more significantly at lower current densities, indicating the formation of HCO_3^- from OH^- and CO_2 and more efficient OH^- utilization due to an excess of CO_2 compared to OH^-. As the current density increases and more OH^- is generated, catholyte products gradually change from HCO_3^- to CO_3^{2-} due to limited CO_2 mass diffusion. Fig. 4d presents the cell voltage and ΔpH_{cat} at various CO_2 concentrations at a fixed current density, demonstrating that increasing the CO_2 levels at the cathode helps push the carbon absorption reaction towards bicarbonate, resulting in lower cell voltages and greater pH drops. The decreasing slope of the upward trend is mainly due to the buffering capacity of (bi)carbonate ions. This demonstrates that the current density and CO_2 concentration not only affect the capture or sorbent generation rate but also modulate the electrochemical environment under the cell conditions.

To quantify how efficiently the regenerated sorbent is used to capture CO_2 in a single-pass flow through the cathode,

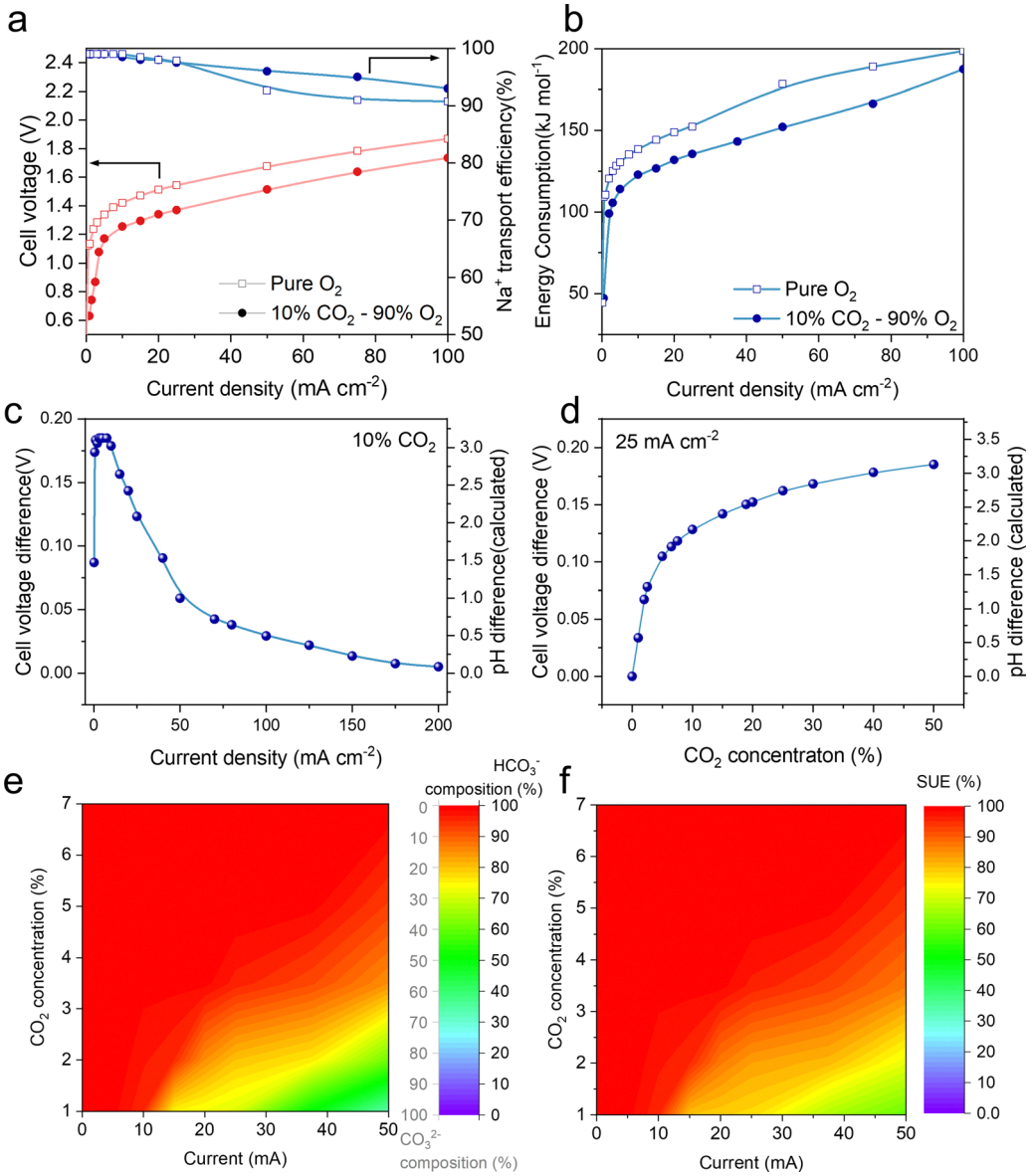

Fig. 4 Effects of the CO_2 feed and cathodic pH on the PSE electrolyzer performance. (a) *I–V* curve and Na^+ transport efficiency. (b) Energy consumption of the PSE electrolyzer with feeds of 10% CO_2-90% O_2 and pure O_2. (c) Cell voltage shifts and the corresponding cathodic pH differences (ΔpH_{cat}) between 10% CO_2 and pure O_2 feeds across varying current densities. (d) Cell voltage shifts and the corresponding cathodic pH differences (ΔpH_{cat}) at 25 mA cm^{-2} across different CO_2 ratios. Here, ΔpH_{cat} represents the difference in the cathodic pH under the CO_2-fed and CO_2-free (pure O_2) operating conditions. The pH differences are derived from the voltage shifts observed when switching from 0% CO_2 (pure O_2 feed) to different CO_2 concentrations at 25 mA cm^{-2}. In both (c) and (d), the right-axis pH values are calculated from the left-axis voltage values, and the plotted curve corresponds to both axes. (e) Distribution of the captured CO_2 species as a function of the CO_2 concentration and current. (f) Sorbent utilization efficiency (SUE) as a function of the CO_2 concentration and current, obtained and processed from experimental data.

we defined the sorbent utilization efficiency (SUE) as follows:

$$\mathrm{SUE} = \frac{[\mathrm{NaHCO_3}] + [\mathrm{Na_2CO_3}]}{[\mathrm{NaOH}]} = \frac{[\mathrm{HCO_3^-}] + [\mathrm{CO_3^{2-}}]}{[\mathrm{Na^+}]} = 1 - \frac{[\mathrm{CO_3^{2-}}]}{[\mathrm{Na^+}]}. \quad (3)$$

The SUE indicates the chemical form in which CO_2 is captured: a 50% sorbent utilization efficiency corresponds to CO_2 being captured as CO_3^{2-}, while a 100% efficiency represents full conversion to HCO_3^-. Importantly, the SUE obtained in this work from titration (Fig. S9) reflects only HCO_3^- and CO_3^{2-} produced from electrochemically generated OH^-, excluding contributions from dissolved CO_2 or H_2CO_3. Thus, the SUE quantifies only the portion of electrochemical OH^- that is converted into bicarbonate or carbonate and not the CO_2 that dissolves without consuming OH^-. When combined with the Na^+ transport efficiency (t_{Na+}), which is characterized by an increase in the Na^+ concentration at the cathode, the overall electron efficiency for CO_2 capture (EE_{CO2}) can be

calculated. EE_{CO2}, defined as the ratio of captured carbon species to the total electrons used, serves as a key metric for evaluating capture effectiveness as follows:

$$\text{CO}_2 \text{ electron efficiency } (\text{EE}_{\text{CO}_2}) = \frac{\text{Total captured carbon}}{\text{Total e}^-} = \frac{n(\text{HCO}_3^-)+n(\text{CO}_3^{2-})}{\text{Total e}^-}, \quad (4)$$

$$\text{EE}_{\text{CO}_2} = t_{\text{Na}-} \times \text{SUE} \quad (5)$$

Assuming t_{Na+} = 100%, the EE reaches 100% for bicarbonate formation and 50% for carbonate formation. This difference arises from the reaction stoichiometry: one bicarbonate reacts with one proton (and thus one electron) to form CO_2, whereas one carbonate requires two protons—one to convert to bicarbonate and another to generate CO_2.

To illustrate how operating conditions influence the sorbent utilization efficiency, we quantified the bicarbonate composition, defined as the ratio of $n(HCO_3^-)$ to total carbon species (measured by acid titration), at various CO_2 concentrations and currents, and then, we visualized captured CO_2 species and sorbent utilization efficiency with contour maps generated from experimental data (for more details, see the SI). As shown in Fig. 4e, higher CO_2 concentrations or lower current densities promote increased HCO_3^- formation. When converted to the sorbent utilization efficiency using eqn (3), Fig. 4f shows how the sorbent utilization efficiency varies with the CO_2 concentration and applied current. Therefore, the cathodic pH difference, which reflects the bicarbonate composition and is a key indicator of the sorbent utilization efficiency, increases at higher CO_2 concentrations but decreases at higher current densities. These results highlight the intrinsic balance between the CO_2 concentration, current density, and cell voltage in determining the performance of the PSE electrolyzer. By carefully matching the input CO_2 concentration and the corresponding operating current density, a high sorbent utilization efficiency can be maintained to deliver high electron efficiency in carbon capture.

PSE electrolyzer performance and stability study for carbon capture

To evaluate the impact of catholyte Na^+ accumulation on reaction efficiency and stability, we first conducted a cation mass balance analysis during the continuous, integrated electrochemical carbon absorption and regeneration process. This involved the continuous flow of the middle buffer chamber stream (1.0 M $NaHCO_3$ at 60.0 mL h^{-1}) and the cathode stream (1.0 mL h^{-1}), as shown in Fig. 5a. At a current of 50 mA, the theoretical increase in the Na^+ concentration in the cathode stream is approximately 1.86 mmol h^{-1}, which should be matched by a corresponding Na^+ decrease in the middle PSE layer stream if the cation mass balance is maintained. This value will be around 1.64 mmol h^{-1} when considering a Na^+ transport efficiency of 88%. According to the ion chromatography result, the Na^+ concentration drops by ~0.0265 M in the PSE layer stream, while the concentration in the cathode stream increases by ~1.65 M, corresponding to 1.59 mmol h^{-1} and 1.65 mmol h^{-1}, respectively. The decrease in the Na^+ amount from the PSE layer stream closely matches the amount detected in the catholyte, confirming the Na^+ mass balance between the middle buffer chamber and the cathode. The sorbent utilization efficiency and electron efficiency were evaluated based on the (bi)carbonate species in the catholyte and t_{Na+}. As shown in Fig. 5b, the SUE and EE for point source capture using 10% CO_2 are higher than 60% and 50% at 200 mA cm^{-2}, respectively. To explore the maximum absorbent concentration that our PSE reactor could achieve in the cathode, we performed an additional experiment with a decreased flow rate of the catholyte at 200 mA (Fig. S11). The Na^+ transport efficiency remains stable at ~85% even when producing a Na^+ concentration as high as 5.0 M at a DI water flow rate of 1.3 mL h^{-1} (together with O_2 as the gas input), suggesting that catholyte Na^+ accumulation has no significant impact on cell performance. However, with a further reduction in the catholyte flow, carbonate salts may crystallize and block the membrane, decreasing the cation transport efficiency, especially considering that the theoretical solubility of Na_2CO_3 is only 2.6 M at room temperature.

The advantages of our three-chamber PSE reactor design can be clearly demonstrated by comparing its intrinsic electrochemical performance with other cell configurations. Compared to a conventional two-chamber membrane electrode assembly (MEA) electrolyzer, where both electrodes directly contact the CEM, the middle chamber in the three-chamber configuration functions as an important "PSE layer" buffer. The "PSE layer" buffer effectively dilutes proton flux at the anode-membrane interface, reducing the proton competition for Na^+ transport across the CEM by separating the acidic and basic interfaces. Moreover, the PSE layer facilitates good ionic conduction in the middle chamber, promoting Na^+ transport across the CEM. As shown in Fig. S12 and S13, after replacing the three-chamber PSE configuration with a two-chamber MEA configuration, the cell voltages increase drastically, suggesting a repulsion effect at the interface, where protons hinder Na^+ transport.

The anodic pH also significantly influences the cell voltage, as discussed above. When the PEM (Nafion membrane) is removed (Fig. S14), the anode is in direct contact with the PSE layer, which results in a cell voltage decrease of approximately 0.5 to 0.6 V. Elevated temperatures generally accelerate the electrolysis process by increasing ion mobility in the electrolyte and facilitating reactions at the electrode surfaces, leading to increased rates of electrochemical reactions. As shown in Fig. S15, an increased temperature yields a lower cell voltage. At 70 °C, the cell voltage decreases by approximately 150 mV at 100 mA cm^{-2}, compared with the cell voltage at room temperature, indicating enhanced reaction kinetics. The energy consumption for flue gas carbon capture with different concentrations is demonstrated in Fig. 5c, with an onset value of ~48 kJ mol^{-1} CO_2. The 2-chamber PSE configuration shows the lowest pH difference but shows increased cost due to the use of the CO_2 and O_2 mixture. Compared with other

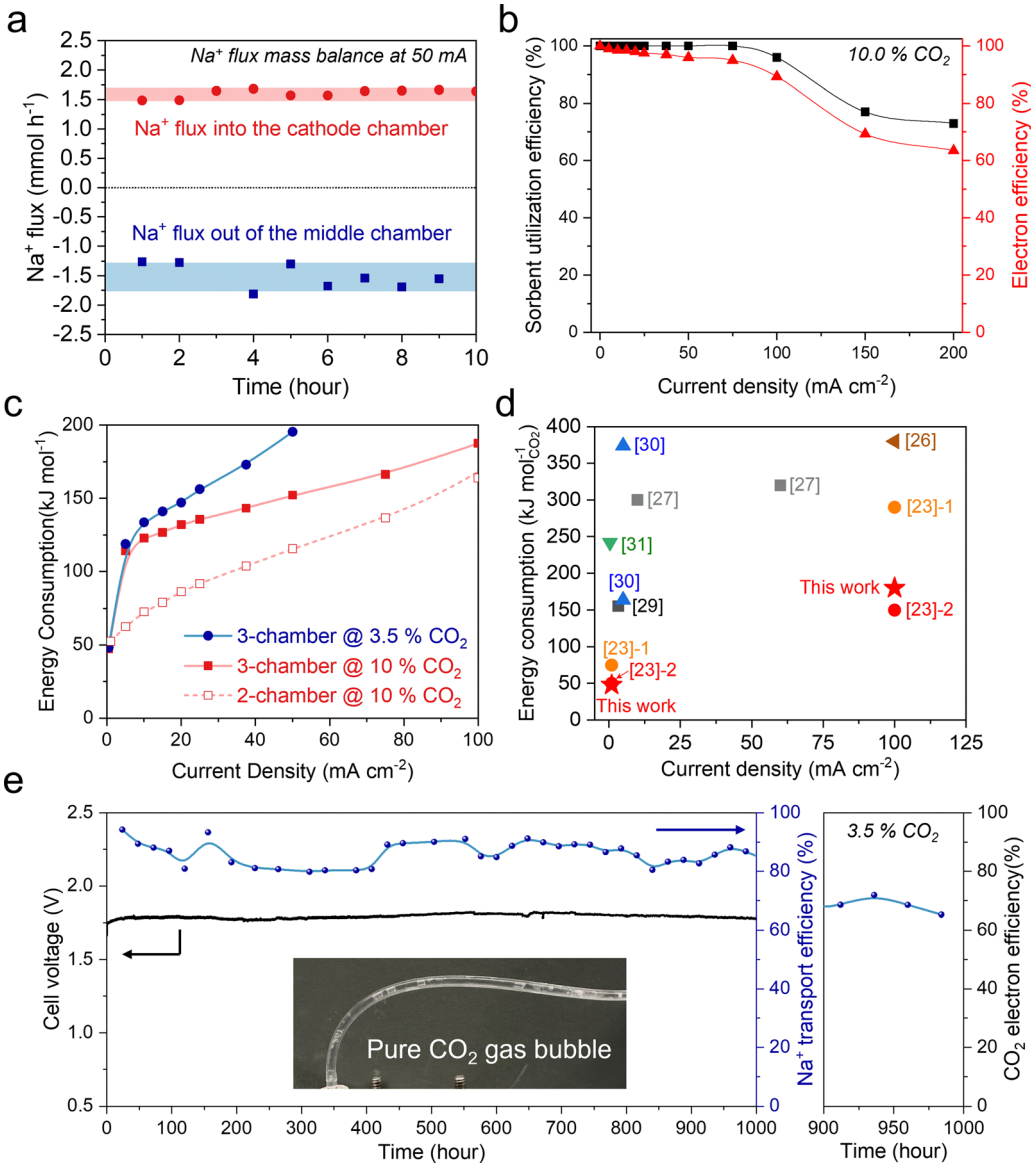

Fig. 5 Electrochemical characterization and stability of the PSE electrolyzer for point source carbon capture. (a) Na^+ mass balance between the middle PSE layer and the cathode. (b) Sorbent utilization efficiency and electron efficiency for point source capture using 10% CO_2. (c) Energy consumption for flue gas carbon capture with different concentrations. Onset: ~48 kJ $mol_{CO_2}^{-1}$ and average: 110–180 kJ $mol_{CO_2}^{-1}$. The 2-chamber PSE configuration shows the lowest pH difference but generates a mixed CO_2/O_2 stream. (d) Comparison of this work and emerging technologies for point source capture: ref [23-1] correspond to the carbonate feed, and ref [23-2] represent the bicarbonate feed, which leads to lower energy consumption.[23,26–28,30,31] Detailed parameters are summarized in Table S3. (e) 1000 hour stability with a 3.5% CO_2 feed at a constant current density of 50 mA cm^{-2}. CO_2 electron efficiency was calculated based on the CO_2 regeneration rate from the middle chamber. The 3-chamber PSE cell demonstrated good stability with a minimal voltage increase.

emerging technologies for point source capture (Fig. 5d), our proposed method shows one of the lowest energy consumptions at higher capture rates.

To evaluate the practical long-term stability of our PSE device for this integrated carbon absorption and regeneration process, we conducted an extended carbon capture experiment (Fig. 5e). The stability was evaluated by applying a constant operating current density of 50 mA cm^{-2}, with a 3.5% CO_2 feed at the inlet of the cathode and 500 mL of a 1.0 M $NaHCO_3$ solution as the starting stock solution for the middle chamber during the whole course of stability testing (flow rate: 60 mL h^{-1}). Please note that this starting carbonate solution can be fully regenerated as CO_2 in 268 hours of operation if no carbon capture is performed to recharge the (bi)carbonate ions. Benefiting from reliable electrocatalysts, membranes, porous solid electrolytes, a less alkaline cathodic condition, and the three-chamber PSE cell configuration, our electrolyzer shows excellent stability in capturing CO_2 at the cathode and regenerating high-purity CO_2 at the middle chamber. The three-chamber PSE reactor can be stably operated for more than

1000 hours, with negligible degradations in both the cell voltage (less than 50 mV increase) and t_{Na+} (maintained at >80% after 1000 hours). No additional (bi)carbonates or alkaline solutions are used during the 1000 hour operation, with pure CO_2 generated from the absorbent (Na_2CO_3 and/or $NaHCO_3$ as captured carbon species), demonstrating the "integrated absorption and regeneration" concept in this study. Under a 50 mA cm^{-2} cell electrolysis current, approximately 32.8 mL of CO_2 can be stably captured as a pure phase in each hour, with an average energy consumption of 235 kJ $mol_{CO_2}^{-1}$ (equivalent to 5.3 GJ ton^{-1}). The slightly higher energy consumption is mainly attributed to the reduced electron efficiency resulting from the lower CO_2 concentration used (3.5% instead of 10%). When scaled up to a 1 m^2 electrode device, this corresponds to a production rate of approximately 14.2 kg of pure CO_2 per day. Notably, this represents a 33% reduction in the energy input compared to the previously reported AEM-CEM PSE reactor system (~350 kJ $mol_{CO_2}^{-1}$ at a similar CO_2 capture rate).[24]

Electrochemical preformation in direct air capture (DAC)

DAC enables the removal of CO_2 directly from the atmosphere, offering a versatile approach to carbon capture independent of emission sources. Building on the robust performance of our PSE device in point source capture, we further explored its applicability for DAC, where atmospheric CO_2 concentrations are significantly lower (~400 ppm). Despite the lower concentration, the same principles of electrochemical reactions and the robust architecture of the PSE electrolyzer ensure effective CO_2 capture. Notably, the cathode's operation in oxygen-rich air allows the oxygen generated at the anode to be collected, enabling the co-production of pure O_2 and pure CO_2.

The electrolyzer behavior differs notably when capturing atmospheric CO_2 (400 ppm) compared to concentrated CO_2 feed streams (Fig. 6a and Fig. S21). At a given current density, flue gas capture operates at a lower cell voltage than atmospheric CO_2 capture. This difference can be attributed to variations in the local pH at the cathode following CO_2

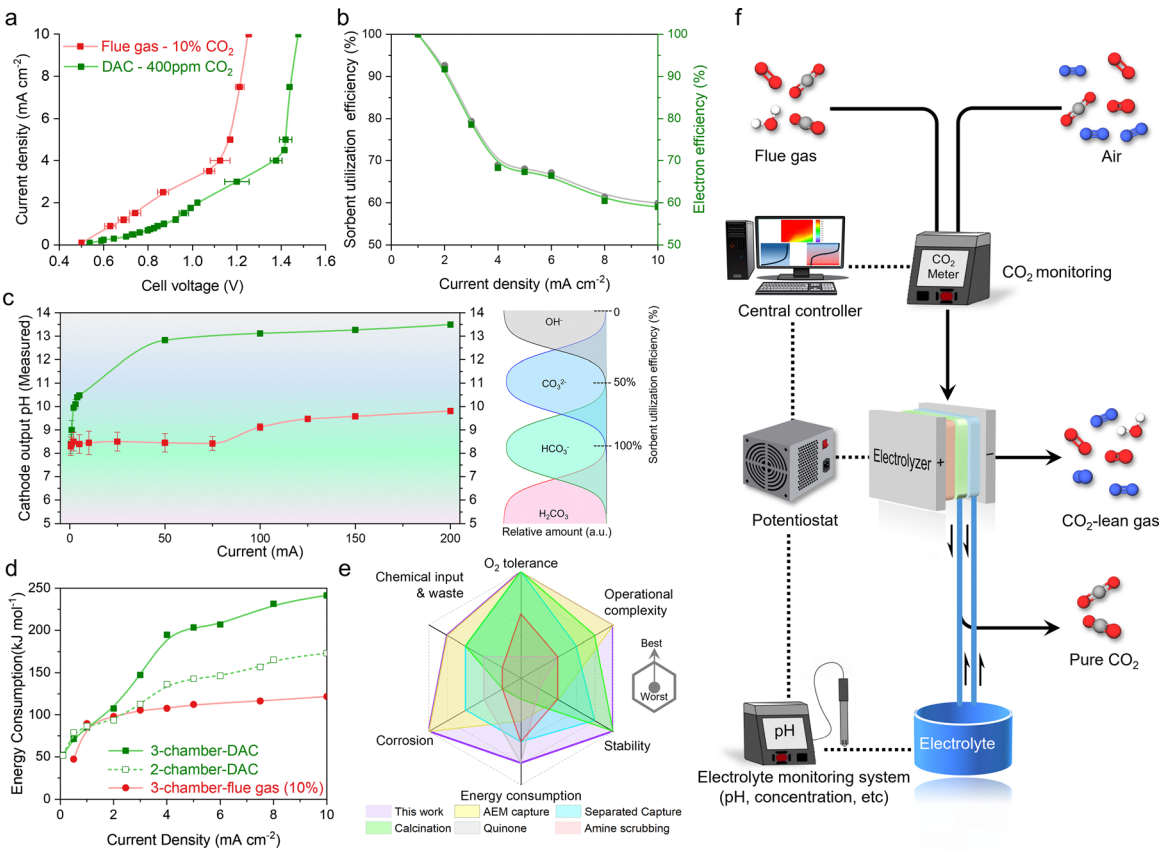

Fig. 6 PSE electrolyzer for direct air capture. (a) *I–V* curves of PSE electrolyzers for CO_2 capture from 10% CO_2 feed gas and atmospheric CO_2. The flue gas capture shows lower cell voltages at the same current density, attributed to the decreased pH at the cathode after CO_2 capture. (b) Sorbent utilization efficiency and electron efficiency for DAC. (c) pH-current diagram of the catholyte outlet for CO_2 capture from 10% CO_2 feed gas and atmospheric CO_2. Flue gas capture occurs at a much lower pH and at the same current, corresponding to the same OH^- concentration. Sorbent utilization efficiency is defined for (bi)carbonates. (d) Energy consumption for direct air capture and flue gas carbon capture. Onset: ~52 kJ $mol_{CO_2}^{-1}$; average: ~150 kJ $mol_{CO_2}^{-1}$ for 2-chamber PSE and ~200 kJ $mol_{CO_2}^{-1}$ for the 3-chamber PSE electrolyzer. (e) Comparison of our proposed carbon absorption and regeneration strategy with other methods using radar charts. (f) Schematic of the proposed dynamic electrochemical CO_2 capture from flue gas or air in our solid electrolyte reactor. The CO_2 and electrolyte monitoring system, which monitors the inlet CO_2 concentration and sorbent utilization efficiency, will be integrated with the potentiostat and central controller to enable dynamic current density control, maintaining electron efficiency and automating the carbon capture process.

absorption (Fig. 4d), where a greater pH shift in the flue gas capture contributes to reduced energy consumption. The sorbent utilization and electron efficiencies for DAC are demonstrated in Fig. 6b. Notably, the CEM-based PSE reactor maintains over 99.5% electron efficiency at 1 mA cm^{-2} and ~70% at 5 mA cm^{-2}, demonstrating its flexibility and adaptability for integrated carbon absorption and regeneration across varying operating conditions. While the electron efficiency is lower in DAC compared to point source capture, this difference primarily arises from the much lower CO_2 concentration in ambient air and the inherently slower capture kinetics. Nonetheless, the high electron efficiency at low current densities highlights the reactor's strong potential for efficient DAC performance. Fig. 6c demonstrates that the electron efficiency is closely tied to the pH of the absorbent. If no CO_2 is captured, the catholyte will contain only OH^-, resulting in an EE of 0%. In contrast, the conversion of bicarbonate requires only one electron per CO_2, compared to CO_3^{2-}, which enhances electron efficiency and reduces the energy demand. Furthermore, at a fixed current and OH^- concentration, flue gas capture results in a more substantial pH drop at the catholyte outlet compared to ambient air capture.

Energy consumptions of the PSE electrolyzer under different conditions are shown in Fig. 6d. For DAC, the system shows onset energies of around 50 kJ $mol_{CO_2}^{-1}$ and ~80 kJ $mol_{CO_2}^{-1}$ at 1 mA cm^{-2}. At a 5 mA cm^{-2} current density, it requires ~150 kJ $mol_{CO_2}^{-1}$ for the 2-chamber PSE electrolyzer and ~200 kJ $mol_{CO_2}^{-1}$ for the 3-chamber PSE configuration. These results show the higher energy demand of DAC compared to flue gas capture, primarily due to the significantly lower concentration of CO_2 in atmospheric air. The system's operational flexibility makes it well-suited for operation near renewable energy sources and geological storage sites, offering a scalable and energy-efficient pathway for CCUS. Further advancement toward practical scalability and economic viability would require progress in several key areas to reduce the overall energy consumption of DAC systems, including: (i) increasing the achievable current density under dilute CO_2 conditions to enhance reaction rates and reduce capital costs, (ii) reducing electrolyzer, membrane, and catalyst costs while improving long-term operational durability, and (iii) increasing the retention time through electrode architecture modification or flow channel design to improve sorbent utilization efficiency and energy efficiency under low-concentration feed streams. By coupling reactive absorption, local pH gradients, and electrochemical regeneration within an integrated system architecture, this strategy may reduce reliance on energy-intensive intermediate steps such as thermal regeneration and separate process units. In principle, the proposed integration could lower balance-of-plant complexity, reduce system-level energy losses, and improve compatibility with modular scale-up. While significant advances in materials and operating conditions are still required, this work highlights a potential pathway toward future, low-cost and scalable carbon utilization systems.

A comparison between our approach and conventional CO_2 absorption and regeneration technologies, such as calcium looping and amine scrubbing thermal, as well as three strategies reported in the recent literature, is provided in the radar plot in Fig. 6e and Table S1. While energy inputs vary across methods, calcium looping is inherently energy-intensive, and many electrochemical strategies suffer from high energy consumption due to low sorbent utilization or large pH overpotentials. In contrast, our integrated CO_2 absorption and regeneration approach operates solely on renewable electricity without any additional chemical input, requires no additional chemical inputs, and generates no waste or pollutants owing to its closed-loop operation and long-term air stability. Notably, unlike the previously reported AEM system, which relies on a carbonate-limited pathway with restricted electron efficiency, point-source-only operation, and CO_3^{2-} transport, the integrated Na-driven CEM system enables direct bicarbonate regeneration, decoupled absorption/regeneration, and fundamentally different ion transport. As a result, the presented system lowers energy consumption (~150 *vs.* ~350 kJ mol^{-1} CO_2), enables practical DAC, achieves up to 90% electron efficiency, and demonstrates >1000 h durability. Unlike traditional methods that separate the carbon absorption from CO_2/sorbent regeneration, our integrated method enables the continuous, simultaneous absorption and regeneration of pure CO_2 (99.5%, determined by gas chromatography, Fig. S22), lowering operational complexity and eliminating complicated pre-/post-treatment such as evaporation or salt dissolution. This simplification may contribute to lower capital costs. Additionally, compared with a separated system, the integrated system maintains a stable operating voltage, ensuring sufficient Na^+ crossover and avoiding high voltage peaks that increase energy consumption. Importantly, the process does not involve strong acids or bases and avoids corrosion issues commonly associated with the amine scrubbing process. Overall, the comparison demonstrates the versatility and potential of our PSE device as a sustainable and scalable solution for both industrial and atmospheric CO_2 capture. The future deployment of the PSE electrolyzer will require considerations beyond the single-cell configuration demonstrated here. In multi-cell stacks, uniform electrolyte distribution, controlled pressure drop, effective gas–liquid management, and parasitic energy demands must be addressed. These challenges can be mitigated by utilizing flow-field and manifold designs that are already established in commercial electrolyzers. Shunt currents can be minimized through appropriate electrical isolation strategies, and parasitic pumping and circulation loads are expected to remain modest due to the system's low pressure drop. The high-purity CO_2 output also enables straightforward integration with downstream CO_2 utilization or storage pathways, supporting practical CCUS implementation. Building on these features, we propose an automated CO_2 capture system that integrates CO_2 and electrolyte monitoring with a potentiostat and a central controller (Fig. 6f). By adjusting the current density in response to the inlet CO_2 concentration and sorbent utilization efficiency, the system can maintain high electron efficiency and minimize energy consumption, enabling fully automated and energy-optimized carbon capture.

Conclusion

In conclusion, we have developed a closed-loop, electrochemical system for integrated CO_2 capture and sorbent regeneration that combines high operational stability with significantly reduced energy consumption. By leveraging in situ-generated concentrated hydroxide at the cathode for direct CO_2 absorption and simultaneously regenerating high-purity CO_2 and the sorbent, our design eliminates the need for separate absorption and regeneration units, streamlining the system architecture and enhancing the overall efficiency. Co-feeding CO_2 with air or O_2 lowers the cell voltage and improves cation transport across the cation exchange membrane, further reducing energy consumption. Through careful tuning of the current density to match the inlet CO_2 concentration, the system predominantly converts CO_2 into bicarbonate under point-source capture conditions, enhancing electron efficiency and reducing energy consumption. This strategy achieves carbon capture at energy inputs as low as $\sim$48 kJ mol^{-1} for onset capture and $\sim$180 kJ mol^{-1} at 100 mA cm^{-2} under flue gas conditions (10% CO_2 concentration) and remains effective for direct air capture with comparable performance. The operational flexibility and long-term stability highlight the potential of our system as a scalable and practical solution for low-cost, high-efficiency CO_2 capture.

Methods

Three-chamber PSE cell configuration and electrochemical measurements

Salt splitting and acid/base generation were conducted in a PSE cell. The cell configuration and operating procedure are illustrated in Fig. 2b and c, respectively. The CEM close to the cathode (cathodic ORR catalyst: Pt/C or Co-SAC on a hydrophobic carbon cloth electrode) was a Nafion N2100TX or ePTFE-reinforced Nafion membrane, and the PEM close to the anode side (anodic OER catalysts on carbon paper, IrO_x or RuO_x on a gas diffusion layer electrode) was the Nafion-117 membrane. The active electrode area was 4.0 or 1.0 cm^2 in this study. In the middle chamber, Diaion (Na) ion exchange resin was employed as the PSE.[2,32] The flow rate at the outlet was calibrated using a measuring cylinder. The cathode side of the cell was provided with a mixture of O_2 and CO_2 gases at different concentrations or the atmosphere for the ORR and CO_2 capture reaction. All the cell voltages in our work were reported without any *iR* compensation. For flue gas capture, a simulated flue gas (CO_2, O_2 or atmospheric air) was prepared as the gas input for the reactor system. All gas flow rates were precisely controlled using mass flow controllers, and the concentration of the mixture was measured and recorded using a CO_2 meter (sensor from CO_2Meter).[1,27] The middle solid electrolyte layer was continuously flowed with the (bi)carbonate electrolyte at 1.0 mL min^{-1}, and the cathode side was circulated with the electrolyte at 1.0 mL h^{-1}.

Synthesis of SACs

The method used for synthesizing the Co-SAC is based on our previously reported method with some modifications.[29] First, 1.0 g of *o*-phenylenediamine, 0.44 g of $CoCl_2$, and 2.0 g of SiO_2 nanoparticle (10–20 nm, Aldrich) templates were mixed in 20 mL of a 1.0 M HCl solution. Then, the mixed solution was sonicated for 0.5 h and stirred for another 0.5 h. Subsequently, 12 mL of the 1.0 M HCl solution, which contained 3.0 g of ammonium peroxydisulfate, that is, $(NH_4)_2S_2O_8$, was added dropwise into the above mixed solution with vigorous stirring. After polymerization in an ice bath for nearly one day, the mixture was dried using a rotary evaporator. Then, the dried powder was annealed under an Ar atmosphere at 800 °C for 2 h. Finally, the product was treated by alkaline (2.0 M NaOH) and acid (2.0 M H_2SO_4) leaching successively to remove SiO_2 nanoparticle templates and unstable Co-based species, respectively, to obtain the Co-SAC. We used the same method to prepare the Ni-SAC. The only difference is that 0.405 g of $NiCl_2{\cdot}6H_2O$ and 1.0 g of SiO_2 were used to synthesize the Ni-SAC. The Fe-SAC was obtained based on the procedure reported in our previous paper.

Contour map generation

To visualize the spatial variation of the CO_2 concentration and current for captured CO_2 species distribution (Fig. 4e) and sorbent utilization efficiency (Fig. 4f), contour maps were generated using experimental data. For nonuniformly spaced points, Shepard interpolation was applied using the XYZ gridding tool to produce a regular Z matrix. The data were then plotted using the *Contour-Color Fill* option, with color scales and levels adjusted to emphasize the distribution of captured CO_2 species and the orbital utilization efficiency.

Author contributions

Z. F. and H. W. conceived the project and designed the experiments. Z. F., J. Z., P. Z., Z. Y., A. E., J. W. and W. P. L. performed the experimental study. Z. F. and H. W. wrote the manuscript with support from all authors.

Conflicts of interest

The authors declare no competing interests.

Data availability

The data that support the findings of this study are available from the corresponding authors upon reasonable request.

Supplementary information (SI): Fig. S1–S27, Tables S1–S3, and supplemental references. See DOI: https://doi.org/10.1039/d6ee01132b.

Acknowledgements

This work was supported by the David and Lucile Packard Foundation (grant no. 2020-71371), the Alfred P. Sloan Foundation (grant no. FG-2021-15638), the Welch Foundation Research

grant (C-2051-20230405), and National Science Foundation (grant no. 2505528).

Notes and references

1 P. Zhu and H. Wang, *Nat. Catal.*, 2021, **4**, 943–951.
2 C. Xia, P. Zhu, Q. Jiang, Y. Pan, W. Liang, E. Stavitski, H. N. Alshareef and H. Wang, *Nat. Energy*, 2019, **4**, 776–785.
3 A. Ozden, F. P. García de Arquer, J. E. Huang, J. Wicks, J. Sisler, R. K. Miao, C. P. O'Brien, G. Lee, X. Wang, A. H. Ip, E. H. Sargent and D. Sinton, *Nat. Sustainable*, 2022, **5**, 563–573.
4 A. Sodiq, Y. Abdullatif, B. Aissa, A. Ostovar, N. Nassar, M. El-Naas and A. Amhamed, *Environ. Technol. Innov.*, 2023, **29**, 102991.
5 L. Shi, Y. Zhao, S. Matz, S. Gottesfeld, B. P. Setzler and Y. Yan, *Nat. Energy*, 2022, **7**, 238–247.
6 L. Jiang, W. Liu, R. Q. Wang, A. Gonzalez-Diaz, M. F. Rojas-Michaga, S. Michailos, M. Pourkashanian, X. J. Zhang and C. Font-Palma, *Prog. Energy Combust. Sci.*, 2023, **95**, 101069.
7 F. M. Brethomé, N. J. Williams, C. A. Seipp, M. K. Kidder and R. Custelcean, *Nat. Energy*, 2018, **3**, 553–559.
8 A. I. Osman, M. Hefny, M. I. A. Abdel Maksoud, A. M. Elgarahy and D. W. Rooney, *Environ. Chem. Lett.*, 2021, **19**, 797–849.
9 Y. Liu, H.-Z. Ye, K. M. Diederichsen, T. Van Voorhis and T. A. Hatton, *Nat. Commun.*, 2020, **11**, 2278.
10 K. M. Diederichsen, Y. Liu, N. Ozbek, H. Seo and T. A. Hatton, *Joule*, 2022, **6**, 221–239.
11 J. M. Barlow and J. Y. Yang, *J. Am. Chem. Soc.*, 2022, **144**, 14161–14169.
12 X. Li, X. Zhao, L. Zhang, A. Mathur, Y. Xu, Z. Fang, L. Gu, Y. Liu and Y. Liu, *Nat. Commun.*, 2024, **15**, 1175.
13 X. Ma, L. Azhari and Y. Wang, *Chem*, 2021, **7**, 2843–2847.
14 K. M. Diederichsen, R. Sharifian, J. S. Kang, Y. Liu, S. Kim, B. M. Gallant, D. Vermaas and T. A. Hatton, *Nat. Rev. Methods Primers*, 2022, **2**, 68.
15 G. Wang, J. Chen, Y. Ding, P. Cai, L. Yi, Y. Li, C. Tu, Y. Hou, Z. Wen and L. Dai, *Chem. Soc. Rev.*, 2021, **50**, 4993–5061.
16 Y. C. Xiao, S. S. Sun, Y. Zhao, R. K. Miao, M. Fan, G. Lee, Y. Chen, C. M. Gabardo, Y. Yu, C. Qiu, Z. Guo, X. Wang, P. Papangelakis, J. E. Huang, F. Li, C. P. O'Brien, J. Kim, K. Han, P. J. Corbett, J. Y. Howe, E. H. Sargent and D. Sinton, *Nat. Commun.*, 2024, **15**, 7849.
17 H. Li, M. E. Zick, T. Trisukhon, M. Signorile, X. Liu, H. Eastmond, S. Sharma, T. L. Spreng, J. Taylor, J. W. Gittins, C. Farrow, S. A. Lim, V. Crocellà, P. J. Milner and A. C. Forse, *Nature*, 2024, **630**, 654–659.
18 S. Jin, M. Wu, Y. Jing, R. G. Gordon and M. J. Aziz, *Nat. Commun.*, 2022, **13**, 2140.
19 S. E. Renfrew, D. E. Starr and P. Strasser, *ACS Catal.*, 2020, **10**, 13058–13074.
20 A. P. Muroyama, A. Pătru and L. Gubler, *J. Electrochem. Soc.*, 2020, **167**, 133504.
21 T. N.-D. Cao, S. W. Snyder, Y.-I. Lin, Y. J. Lin, S. Negi and S.-Y. Pan, *Ind. Eng. Chem. Res.*, 2023, **62**, 20979–20995.
22 Y. Xu, S. Liu, J. P. Edwards, Y. C. Xiao, Y. Zhao, R. K. Miao, M. Fan, Y. Chen, J. E. Huang, E. H. Sargent and D. Sinton, *Joule*, 2023, **7**, 2107–2117.
23 X. Zhang, Z. Fang, P. Zhu, Y. Xia and H. Wang, *Nat. Energy*, 2025, **10**, 55–65.
24 Z. Fang, P. Zhu, X. Zhang, Y. Feng and H. Wang, *Nat. Chem. Eng.*, 2025, **2**, 142–151.
25 Y. Feng, Y. Park, S. Hao, Z. Fang, T. Terlier, X. Zhang, C. Qiu, S. Zhang, F. Chen, P. Zhu, Q. Nguyen, H. Wang and S. L. Biswal, *Proc. Natl. Acad. Sci. U. S. A.*, 2024, **121**, e2410033121.
26 I. A. Digdaya, I. Sullivan, M. Lin, L. Han, W.-H. Cheng, H. A. Atwater and C. Xiang, *Nat. Commun.*, 2020, **11**, 4412.
27 P. Zhu, Z.-Y. Wu, A. Elgazzar, C. Dong, T.-U. Wi, F.-Y. Chen, Y. Xia, Y. Feng, M. Shakouri, J. Y. Kim, Z. Fang, T. A. Hatton and H. Wang, *Nature*, 2023, **618**, 959–966.
28 A. P. Muroyama and L. Gubler, *ACS Sustainable Chem. Eng.*, 2022, **10**, 16113–16117.
29 Z.-Y. Wu, M. Karamad, X. Yong, Q. Huang, D. A. Cullen, P. Zhu, C. Xia, Q. Xiao, M. Shakouri, F.-Y. Chen, J. Y. Kim, Y. Xia, K. Heck, Y. Hu, M. S. Wong, Q. Li, I. Gates, S. Siahrostami and H. Wang, *Nat. Commun.*, 2021, **12**, 2870.
30 Q. Shu, L. Legrand, P. Kuntke, M. Tedesco and H. V. M. Hamelers, *Environ. Sci. Technol.*, 2020, **54**, 8990–8998.
31 M. D. Eisaman, K. Parajuly, A. Tuganov, C. Eldershaw, N. Chang and K. A. Littau, *Energy Environ. Sci.*, 2012, **5**, 7346–7352.
32 C. Xia, Y. Xia, P. Zhu, L. Fan and H. Wang, *Science*, 2019, **366**, 226–231.

